PAPER • OPEN ACCESS

The effect of metal-oxide incorporation on the morphology of carbon nanostructures

View the article online for updates and enhancements.

IOP ebooks™

Bringing you innovative digital publishing with leading voices to create your essential collection of books in STEM research.

Start exploring the collection - download the first chapter of every title for free.

The effect of metal-oxide incorporation on the morphology of carbon nanostructures

Sebastian Tigges[1,3] (ID)**, Nicolas Wöhrl**[1,3] (ID)**, Ulrich Hagemann**[1,2] (ID)**,
Marcel Ney**[1] **and Axel Lorke**[1] (ID)

[1] Faculty of Physics and Center for Nanointegration Duisburg-Essen, University of Duisburg-Essen, Duisburg, Germany
[2] Interdisciplinary Center for Analytics on the Nanoscale (ICAN), University of Duisburg-Essen, Duisburg, Germany

E-mail: sebastian.tigges@uni-due.de (S Tigges) and nicolas.woehrl@uni-due.de (N Wöhrl)

Abstract

Metal-organic, single-source, low-temperature, morphology-controlled growth of carbon nanostructures is achieved, using an inductively coupled plasma-enhanced chemical vapor deposition system. Three distinctive morphologies, namely nanoflakes, nanowalls (CNWs) and nanorods (and intermediates between these morphologies), can be reproducibly deposited, depending on the process parameters. The synthesized structures can be described as hybrid materials consisting of metal oxide incorporated in a carbon matrix material. Since the incorporation of metal oxide into the carbon structure significantly influences their growth, the synthesis cannot be described solely with the existing models for the growth of CNWs. Optical emission spectroscopy is used to measure the relative number density of suspected growth and etching species in the plasma, while physical and chemical surface analysis techniques (scanning electron microscopy, Raman spectroscopy, scanning Auger microscopy and x-ray photoelectron spectroscopy) were employed to characterize the properties of the different nanostructures. Therefore, by using methods for both plasma and surface characterization, the growth process can be understood. The precursor dissociation in the plasma can be directly linked to the deposited morphology, as the incorporation of Al_2O_3 into the nanostructures is found to be a major cause for the transition between morphologies, by changing the dominant type of defect within the carbon structure.

Keywords: metal oxide incorporation, morphology transition, plasma-enhanced chemical vapor deposition, carbon nanostructures, carbon nanowalls, nanorods, nanoflakes

S Supplementary material for this article is available online

(Some figures may appear in colour only in the online journal)

---

[3] Author to whom any correspondence should be addressed.

Abbreviations

CNW(s)	Carbon nanowall(s)
PE-CVD	Plasma-enhanced chemical vapor deposition
OES	Optical emission spectroscopy
RF	Radio frequency
SEM	Scanning electron microscopy
SAM	Scanning Auger microscopy
XPS	X-ray photoelectron spectroscopy
UHRSEM	Ultra-high resolution scanning electron microscopy
Pos(x)	Position (Raman shift) of peak x
FWHM(x)	Full width at half maximum of peak x
$I(x)$	Intensity of peak x
CCD	Charge-coupled device
UHV	Ultra-high vacuum
BWF	Breit–Wigner-Fano line shape
SGL	Single Gaussian/Lorentzian mixed line shape

1. Introduction

Carbon nanowalls (CNWs), sometimes called vertically-aligned graphene nanosheets, are a particular form of mostly multilayered graphene, which stands perpendicular on the substrate surface. First reported by Wu *et al* in 2002 [1], their unusually good thermal, electronic as well as mechanical properties combined with adjustable surface area and exposed, sharp edges make them an almost ideal material system for the use in energy conversion [2–4], charge storage [5–7] and field emitter applications [8–10]. Many fields of application for CNWs are very similar to those of the conventionally used carbon allotropes, such as graphene and carbon nanotubes, however, due to the CNWs' vertical alignment, they bring the added benefit of adjustable, absolute surface area (by CNW height). Furthermore, CNWs can be used as a template material for growing other types of nanostructured materials and for nanoimprint [11]. Plasma-enhanced chemical vapor deposition (PE-CVD) of CNWs has been studied by several groups using different excitation energies (microwave, radio frequency, direct current, and combinations of these) and a variety of different set-ups [12, 13]. PE-CVD is a promising method, as it provides industrial-size scalability as well as remarkably low-temperature growth, which enables the use of temperature-sensitive materials (such as polymers) as substrates through the dissociation of the precursor in the plasma. Comprehensive reviews on CNW synthesis, properties, and application, can be found in Bo *et al* [12] and more recently in Santhosh *et al* [13].

Many different attempts have been made to understand the underlying growth mechanism of CNWs, including the works of Zhao *et al* [14], Zhu *et al* [15], Kondo *et al* [16], Davami *et al* [17] and Baranov *et al* [18]. The growth models of CNWs, grown from various precursors and in different configurations, have in principle three stages in common: (1) formation of the so-called buffer layer, a carbon interface layer that initially forms on the substrate [14, 16, 19], (2) creation of nucleation sites (carbon nanoislands) for CNW growth through ion bombardment [16] and/or surface stress [14, 15, 20]

and therefore the transition to the (3) finite vertical growth of CNWs, influenced by the shadowing effect [16], a strong localized electric field at the edges of the CNWs [21], as well as ion bombardment and surface diffusion [18, 22–24]. Thus the growth of CNWs can mainly be influenced by a set of process parameters, which are chamber pressure, gas flow rates (of both carrier/background gas and precursor), excitation power, substrate temperature, and substrate bias [12, 13]. Additionally, the ratio of suspected growth species (C_2, CH and higher mass ions C_xH_y) to amorphous carbon (a-C) etchants (Ar, O, H, N, OH), which feature a higher etching rate for out-of-plane carbon resulting in an anisotropic growth, plays a significant role in the formation of CNWs [15, 16, 25–28]. The different growth mechanisms proposed until now have been discussed in more detail by others [12, 13]. So far, mostly simple precursor compounds, such as low-weight hydrocarbons and fluorocarbons [12, 13], have been used in the literature. Apart from the works of Lehmann *et al* [3, 29, 30], only our group has investigated the possibility of growing CNWs from more complex, higher weight, metal-organic precursors [23, 31] to investigate upon the change in nature of the growth process resulting from the presence of metal oxide during the synthesis.

As CNW growth is an uncatalyzed process, precursor dissociation plays an important role [14, 32]. In the present work, morphology-controlled growth was observed depending on carrier gas flow rate and chamber pressure. Three different morphologies were deposited at relatively low substrate temperatures of 350 °C and classified by scanning electron microscopy (SEM), Raman spectroscopy, scanning Auger microscopy (SAM) and x-ray photoelectron spectroscopy (XPS), namely nanorods, CNWs, and nanoflakes. Characteristic plasma chemistry was found for the individual morphologies as observed by OES. The metal oxide present during synthesis, resulting from the use of a metal-organic precursor in comparison to the use of traditional hydrocarbons, is expected to have a significant influence on the growth of the nanostructures. By combining physical and chemical analysis with the characterization of plasma chemistry, we develop a growth model for the single step, morphology-controlled growth of metal oxide/carbon hybrid nanostructures from a metal-organic precursor in PE-CVD, which identifies the metal-oxide incorporation, directly controlled by the precursor residence time inside the plasma $\tau = k \times \frac{p}{Q}$ [33], as a fundamental synthesis parameter.

2. Experimental methods

2.1. Synthesis

As substrate material laser cut, double-side polished, 200 μm thick, $1 \times 1 \, cm^2$ sized, undoped silicon sold by Siegert Wafer GmbH (batch number: BB14004) was used. As precursor material aluminum acetylacetonate (Al(acac)$_3$) from Sigma-Aldrich Chemie GmbH of the grade 'ReagentPlus'(99%) was used. The substrate or in some cases substrates were placed on top of the substrate holder at a marked position

J. Phys. D: Appl. Phys. **53** (2020) 145206

S Tigges *et al*

and aligned. The chamber was evacuated to $<5 \times 10^{-6}$ mbar before synthesis by a Pfeiffer TC600 turbo molecular pump backed by a forevacuum pump. The synthesis system is an inductively-coupled PE-CVD system excited by 13.56 MHz RF constructed after the guidelines of the gaseous electronics conference reference cell reactor [34] with a specially modified planar plasma antenna to increase plasma densities at low particle energies [35] and slightly modified chamber geometry. For every sample presented here RF power was kept constant at 500 W (real power inside the chamber). Generally, process time was 50 min if not stated otherwise. This time was found sufficient for all of the observed morphologies to nucleate and evolve completely. A bias voltage was applied to the substrate holder and its pulse was modulated to be of a rectangular shape with $+30$ V positive pulse for 0.5 ms and -30 V negative pulse for 5 ms to accelerate ionic species from the plasma onto the substrate. The precursor was evaporated at a constant oven temperature of 100 °C and argon carrier gas was used to carry the evaporated precursor into the reaction zone. The precursor flow rate can be assumed as constant at 0.166 ± 0.01 sccm. Carrier gas flow rate was adjusted as needed using a mass flow controller (MF1 by MKS Instruments Deutschland GmbH). Chamber pressure was adjusted independently of the carrier gas flow rate by using a throttle valve leading to the pumping system, and monitored by two independent pressure gauges, a Pfeiffer ITR 90 and a Leybold CTR100 N. The substrate and precursor were heated to the required temperatures prior to processing.

A more detailed synthesis procedure can be found in the supporting information (stacks.iop.org/JPhysD/53/145206/mmedia).

2.2. Characterization

A detailed description of the characterization and evaluation techniques used in this work can be found in the supporting information.

During synthesis, optical emission spectroscopy (OES) and actinometry were used for the identification of light-emitting species in the plasma to give insight into the plasma chemistry. The set-up used consists of an iStar 340T Series CCD-camera fitted to a Shamrock 303i spectrograph covering the wavelength range from 300 to 800 nm. For structural characterization of the deposited layers, such as the identification of morphology, samples were taken to a scanning electron microscope (SEM; Inspect F and Helios 600 NanoLab DualBeam, FEI Deutschland GmbH). Raman spectroscopy was performed with a green laser (532 nm, laser power below 1 mW) in a Renishaw confocal inVia Raman microscope on all samples. The spectra were evaluated by using the method of Eckmann *et al* [36] for the identification of defect density and type and a standard data evaluation software (Origin). A PHI Versaprobe II was used to record XPS wide scan spectra in a binding energy range of 0–1200 eV. Narrow scan spectra were recorded in the regions of the C1s (around 284 eV), O1s (around 532 eV), N1s (around 400 eV), Al2p (around 72 eV), Si2p (around 100 eV) and the Auger transition of C_{KVV}

(around 1220 eV). All of the spectra shown in this study were fitted with the software CASA XPS according to the method described in the supporting information, while atomic percentages were determined with the software Multipak.

Identification of the chemical composition of a samples' surface with a high lateral resolution (~20–30 nm) was done by using a scanning Auger microscope (SAM). The system used was a PHI 710 Auger electron spectroscope. The samples were measured under 90° tilt and narrow scans of the C1, O1, Al2, and Si2 regions were recorded alongside the growth direction of the wall. Atomic percentages were determined by using the software Multipak.

3. Results and discussion

3.1. Influence of process parameters on nanostructure morphology

In the set-up used in this work, the chamber pressure and argon carrier gas flow rate (in the following referred to as 'gas flow rate') have a significant influence on the morphology of the deposited layers. Three distinct nanostructures and their intermediates (mixtures of two nanostructures) were deposited at relatively low substrate temperatures of 350 °C and observed in SEM. Figure 1 shows the dependence of the morphology of the deposited layer on pressure and gas flow rate (later referred to as residence time). At high gas flow rates and low pressures, nanorods are formed on the Si-substrate. At average gas flow rates and pressures, CNWs are found. At low gas flow rates and high pressures, nanoflakes are deposited, which in some cases look similar to CNWs, but have lost their vertical-alignment almost fully. Furthermore, the overall density of structures increases with increasing gas flow rate and decreasing pressure. The wall thickness increases significantly from nanoflakes to nanorods, especially during the transition from CNWs to nanorods (CNW-nanorod intermediate).

As the gas flow in the employed set-up is parallel to the substrate holder, rather than perpendicular as in other cases [25], not only a single nanostructure is deposited across the length of a sample. Instead, depending on process parameters, multiple nanostructures and their intermediates are deposited on the substrate surface depending on the distance from the gas inlet. Figure 2 shows SEM images of the morphologies of three samples produced in three individual processes of identical process parameters, which were positioned at different distances from the precursor gas inlet. For these and every other sample in this study, nanorods were always deposited closest to the gas inlet, while nanoflakes were always deposited farthest from the gas inlet. CNWs were found in between these two morphologies and intermediates between the three nanostructures were found to form in between the corresponding nanostructures.

Figure 3 shows samples synthesized with different process times (30 to 150 min). After initial nucleation, CNWs seem to continue to grow in a V-like shape, increasing wall length and height until they meet other walls. As CNWs are found randomly oriented on the substrate, the mean wall length (not height) is anti-proportional to nucleation density,
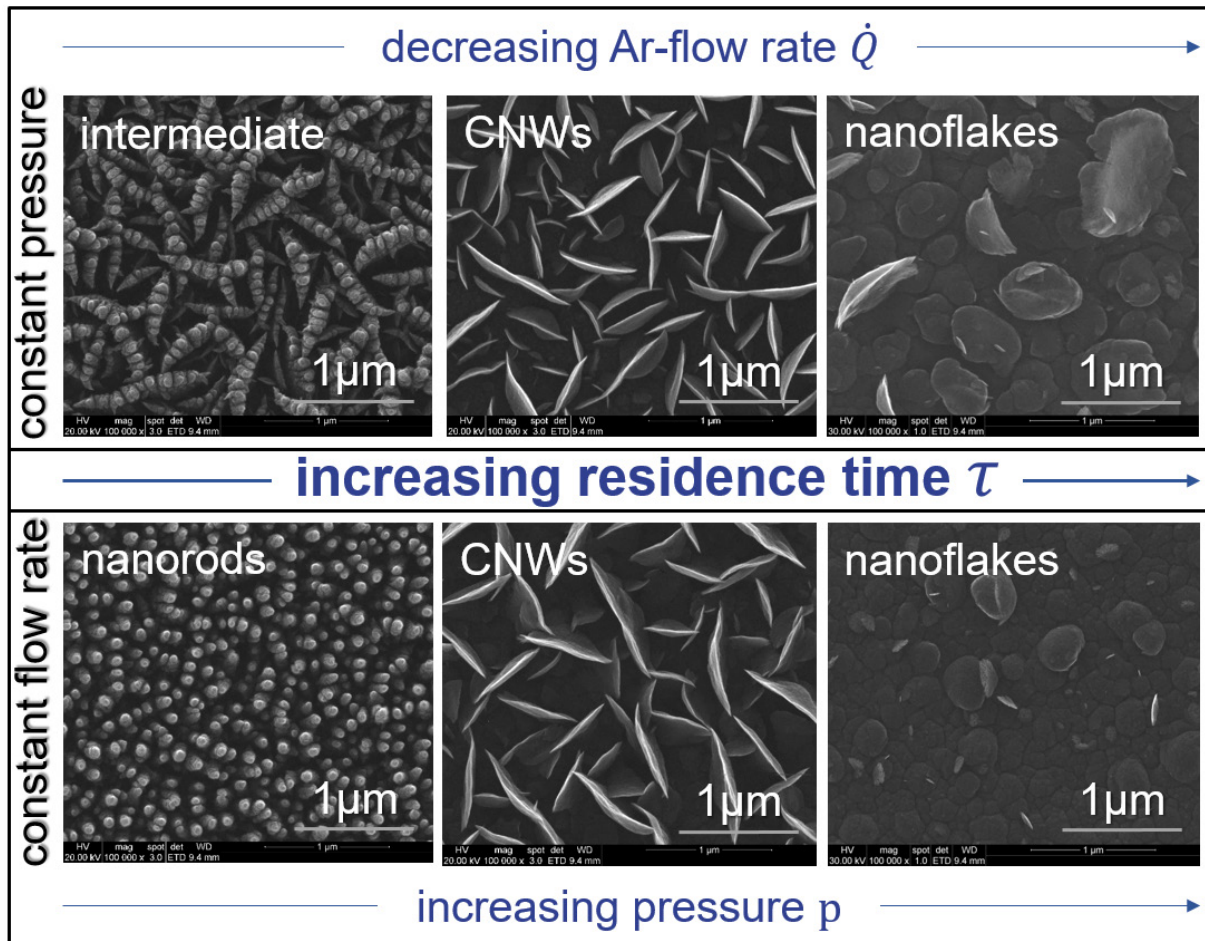
J. Phys. D: Appl. Phys. **53** (2020) 145206

S Tigges *et al*

Figure 1. SEM images of different morphologies deposited at varying pressure and carrier gas flow rate. The residence time of precursor in plasma increases with pressure and decreases with the carrier gas flow rate.
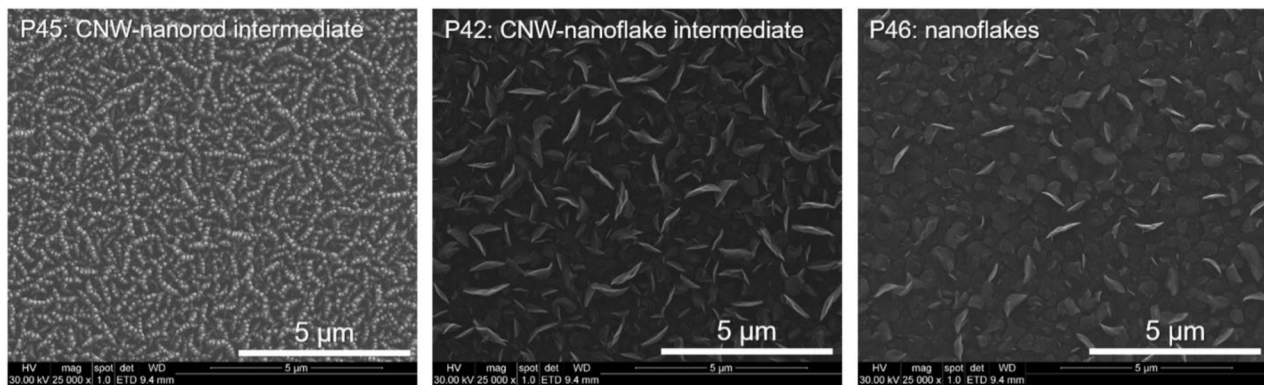

Figure 2. SEM images of the samples processed at a different distance to the gas inlet (P45 closest, P46 farthest from gas inlet; P42 in the middle of P45 and P46). The morphology is dependent on distance to the gas inlet.

which was observed previously [23, 37]. An almost linear increase in wall height is observed. A difference in the height of individual CNWs on the same sample may be attributed to the shadowing effect discussed by Kondo *et al* [16].

In figure 3, it can also be observed that there are no changes in morphology over time. Beyond a certain nucleation time, the CNW and nanoflake structures only continue to grow in length and height, at least until the maximum process time of 150 min. Hence, the three nanostructures observed in this study are individual morphologies growing independent of each other. Based on the observations made until now, it is safe to assume that the nanostructures grow in specific, overlapping growth zones, which form alongside the direction of gas flow and favor the growth of a specific nanostructure.
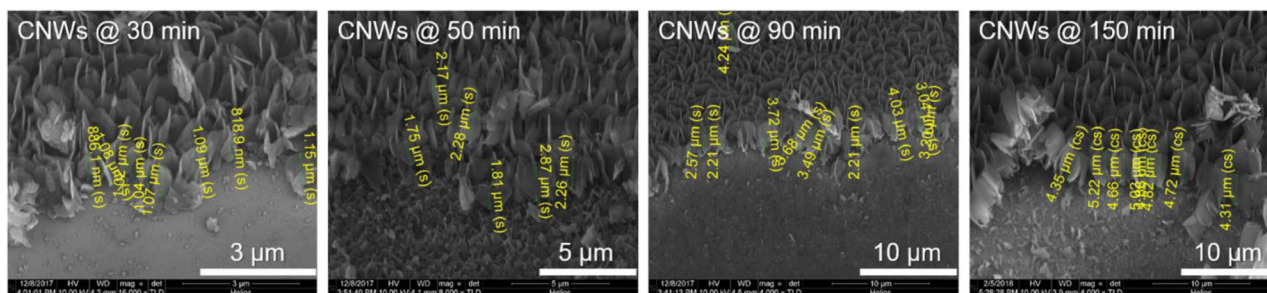
J. Phys. D: Appl. Phys. **53** (2020) 145206

S Tigges *et al*

Figure 3. SEM images of four different samples under 45° tilt to allow measurement of wall height. The wall height increases almost linearly with process time.

3.2. Limited applicability of traditional growth models on the observed morphology transitions

An inhomogeneity in morphology across the samples grown at low substrate temperatures (350 °C) is in agreement with the results of Baranov *et al* who have theorized, that at low temperatures the growth is likely to be dominated by adsorption from the gas phase [18]. This results in a more significant impact of the degree of dissociation of the precursor in the gas phase on the deposited morphology. The impact of substrate temperature on the morphology of the deposited layer was briefly investigated. It was found that higher substrate temperatures benefit the homogeneity of the deposited layers (only CNWs are deposited) greatly. A short discussion can be found in the supporting information.

Morphological changes in CNWs and other carbon nanostructures synthesized with low-weight hydrocarbons have been extensively researched by Vizireanu *et al* [25, 38] and Cho *et al* [26], and particular interest has been put on plasma chemistry analyzed by OES and actinometry. Vizireanu *et al* investigated the structural dependence of their CNWs on the substrate temperature, gas flow rates, radiofrequency (RF) power [38] and distance of substrate to precursor inlet (injection point) [25] with a mixture of $Ar/H_2/C_2H_2$ in a low pressure expanding RF plasma. They have concluded that mainly higher mass ions, which form due to dissociation of precursor and recombination processes of carbon and hydrogen radicals inside the plasma, contribute to the growth of high-quality CNWs. Most importantly, the dissociation of precursor and therefore, the ratio of growth to etching species is dependent on the injection point. Similarly, Cho *et al* linked the pressure and RF power dependent density of their CNW structures to the CH radical and H atom density measured by actinometry. For them, both densities and therefore, the ratio of growth to etching species play an essential role in the formation and quality of CNW films. Others have made similar observations on the morphology-controlled growth by variation of gas ratio, flow rates, and chamber pressure [39, 40].

With the observations and assumptions presented in this study so far, one may assume that the morphologies form depending on the degree of dissociation of the large precursor molecule in the plasma, similar to the results for low-mass precursors from the literature presented above. In general, atomic carbon, the simple carbon dimer C_2 and several low- and medium-mass hydrocarbons are suspected of being the main growth species of CNWs [25, 26, 29, 41]. With increasing

distance to the gas inlet, the precursor gas molecules spend more time in the dissociative environment of the plasma (often referred to as residence time) before reaching the sample surface. Likewise, with increasing pressure and decreasing gas flow rate, the residence time increases. As nanorods are found at plasma conditions, that cause a lesser degree of precursor dissociation (low pressures, high carrier gas flow rates, and close to gas inlet), it is reasonable to assume a hydrocarbon of higher mass as the primary growth species for this morphology. The relatively large (high-mass) precursor $Al(acac)_3$ used in this work inhabits all the necessary bonds for direct dissociation of growth species mentioned above. Due to the large mean free path in the gas (several centimeters) and the low diffusion length on the surface at a low temperature the influence of recombination processes, in the gas phase or on the surface, on the formation of growth species is negligible.

The residence time is an essential parameter to understand dissociation driven processes and their influence on the deposited structure. It is given by $\tau = k \times \frac{p}{\dot{Q}}$, with τ as residence time, p as pressure, $\dot{Q}$ as gas flow rate and k as a constant dependent on chamber geometry [33]. To further substantiate the theory on how precursor dissociation impacts layer morphology, a brief investigation on the influence of the precursor gas flow rate on the morphology of the deposited layer has shown, that a higher precursor gas flow rate, controlled by the oven temperature, shifts the growth zones in the direction of gas flow (see supporting information).

The observation of the distance, pressure and gas flow-dependence of the different morphologies and ultimately the observation of growth zones validates the assumption of a significant influence of the dissociation of precursor on the deposited morphology depending on residence time. So far, traditional growth models and observations in the literature may explain changes in CNW thickness and density, but are not able to explain the observed transitions between morphologies (from nanoflakes to nanowalls to nanorods).

In recent publications, nanorod and CNW deposition (or rather a morphology transition) depending on precursor gas flow rate has been observed for an aromatic precursor by Lehmann *et al* [29] and also for the simpler precursor C_2H_2 by Acosta Gentoiu *et al* [42]. Lehmann's observation of the dependence of morphology on precursor gas flow rate agree with the observations made in this study. The formation of different nanostructures at varying precursor gas flow rate was attributed to the reaction kinetics of two reaction pathways of
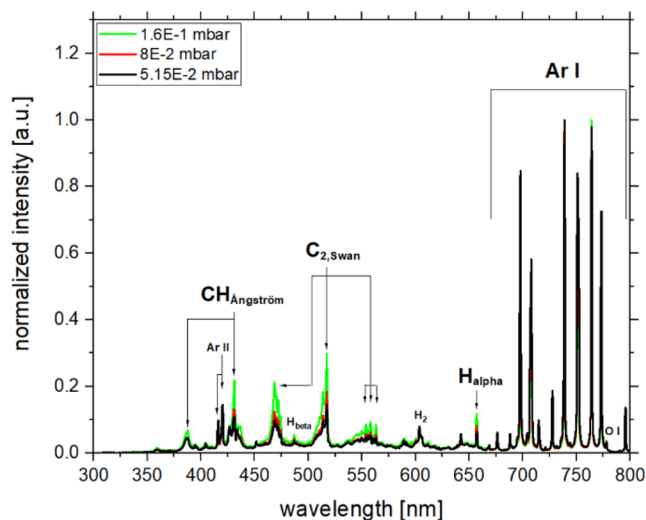
Figure 4. Three typical OES spectra taken at varying pressures. The peaks are labeled according to the species of origin and band name, respectively. An evolution of the C_2/Ar-, CH/Ar-, H/Ar- and O/Ar-ratios with pressure is observable. Peaks have been normalized to the highest Ar-peak in the spectrum.

Table 1. Emission lines evaluated in this study and the references in which they were identified or used in actinometry.

Emission line	Excitation energy (eV)	Reference
Ar at 750nm	13.48	[26, 49]
CH at 431nm	14.6	[26]
C_2 at 516nm	n.a.	[25, 38]
H_α at 656nm	12.1	[26, 49]
O at 777nm	10.74	[49, 50]

their aromatic carbon precursor p-xylene. However, they did not explain the morphology transition in detail.

The formation of nanorods instead of CNWs must result from a transition in the general dimensionality of the growth mechanism [43]. The traditional growth mechanism proposed in the literature suggests, that this transition may only result from a change in the ratio between amorphous carbon etchants (H_2, O_2, and Ar) and growth species (C_2 and hydrocarbons). Especially when considering the observation that walls grow wider before they reach the nanorod growth regime (CNW-nanorod intermediate) and when assuming that surface diffusion rates stay similar across all low-temperature process parameters. Further understanding of the underlying growth mechanism, therefore, requires an insight into the plasma chemistry during deposition.

OES and actinometry were employed to investigate the plasma chemistry during the deposition and further validate a dissociation-driven process being responsible for the formation of different morphologies on the samples with the residence time being a fundamental parameter.

Actinometry is a method capable of determining the ratios of reactive species in the plasma and in some cases even the number density. In the original publication of Coburn and Chen *et al* [44], it was demonstrated, that the intensity of the optical emission of a particular species is directly correlated to its density in the plasma and the electron energy distribution function. In this method, a known amount of inert gas (here argon) is supplied to the plasma system. Determining the ratio of intensities between a reactive species and an argon emission line yields the theoretical amount of reactive species in the plasma.

Typical OES spectra at different pressures are shown in figure 4. The peaks used and discussed in this paper are CH at 431nm, C_2 at 516nm, H_α at 656nm, O at 777nm and Ar at 750nm. The excitation energies taken from the literature,

where actinometry of these lines was used, can be found in table 1. A value for C_2 was not found in the literature, but the emission line of C_2 has been successfully used before [25, 41]. Further explanation of the OES actinometry procedure can be found in the supporting information.

Since the direct dissociation of the precursor in the plasma of our set-up is dominant because of the long mean free path, for the scope of this paper, it is crucial that acetone, ethanol, and water is formed in the gaseous phase, which was proven by others [45–49]. All of these products incorporate the necessary bonds for direct formation of the growth species C_2 and CH and the a-C etchants H and O.

In figure 4, a pressure-dependent variation in the ratios of reactive species to noble gas can already be observed, which is further illustrated in figure 5. As mentioned before, the residence time increases with increasing pressure and decreasing gas flow rate, which results in a higher degree of precursor dissociation. With increasing pressure (at constant gas flow rate) the signals of both growth species, CH and C_2, and a-C etchants, H and O, increase. This effect is observed here, because all of the reactive species shown in figure 5 may only be produced from direct dissociation of the precursor. The same trend is observed with decreasing gas flow rates (at constant pressure).

The ratio of the sum of a-C etchants to each of the growth species can be extracted from figure 5 and is displayed in figure 6 for varying pressure and constant gas flow rates. The sum of a-C etchants is taken into account as both H and O chemically etch a-C and out-of-plane carbon in a similar manner, and, therefore, contribute to the anisotropic growth of CNWs. In figure 6, decreasing ratios can be observed for increasing pressures. The almost horizontal progression of the ratios at a constant gas flow rate of 93 sccm are expressed by the resulting morphologies, as they are identical from 12.5 Pa onwards to higher pressures. For decreasing gas flow rates and constant pressures, the ratio of a-C etchants to growth species also decreases, but not as apparent. This is possibly due to the increase in argon proportion in the gas composition, that should result in a similar increase in the etching of a-C by kinetically removing loosely bonded out-of-plane carbon [13], even though less H and O seem to be present.

In any case, more a-C etchants in relation to growth species introduced into the system should result in more a-C etching and crystalline, anisotropic CNW growth, while the opposite is observed in this work. This contradicts the model proposed in the literature, where a higher proportion of a-C etchants is thought of being a significant driver of crystalline CNW
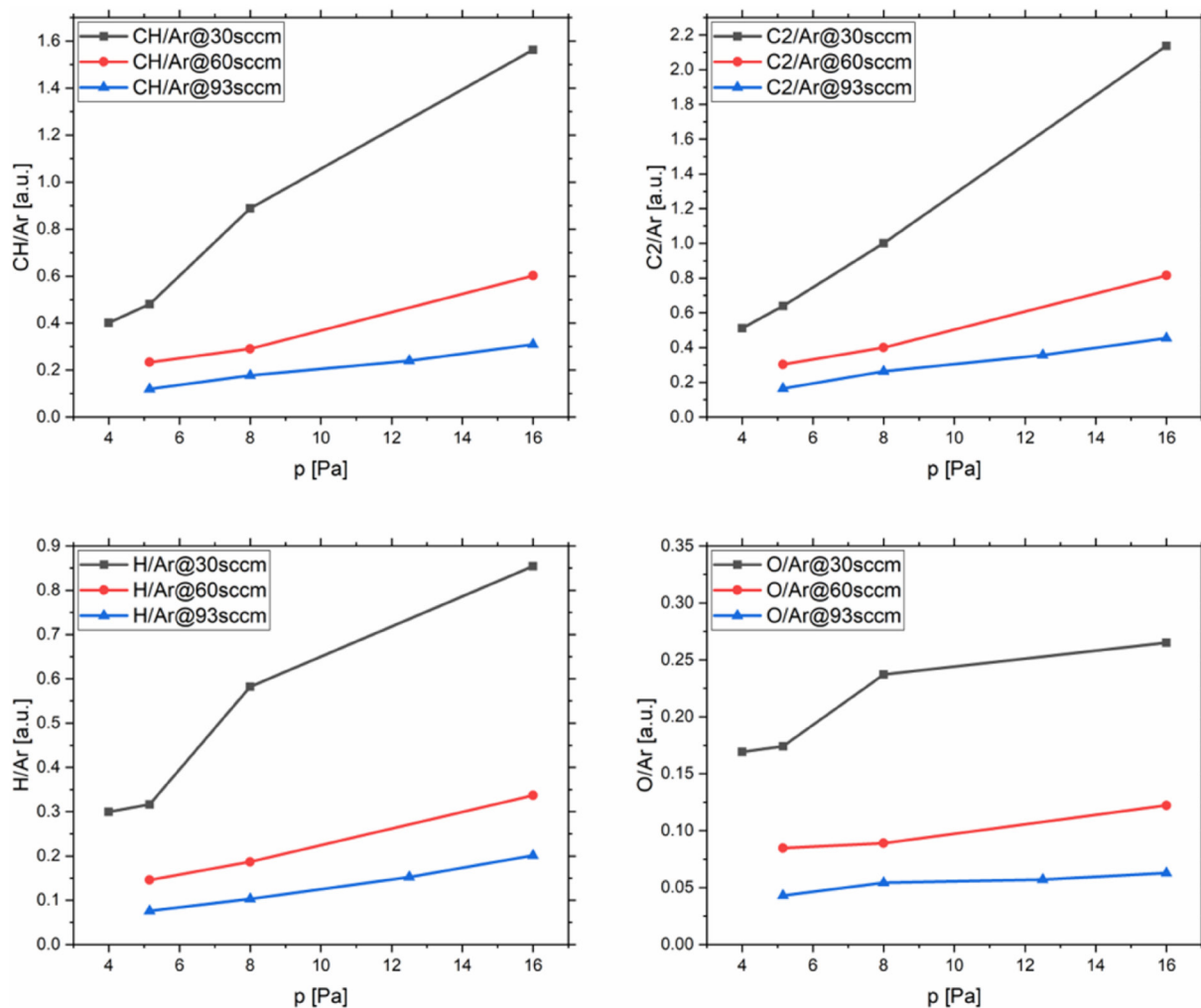
Figure 5. The ratios of relevant growth and etching species taken from OES spectra at different process pressures. As expected, all of the ratios increase with pressure, as the residence time increases. Similar trends are observed for decreasing carrier gas flow rate (not shown here).

growth [13, 16, 27, 28] and thickness should be reduced by hydrogen induced etching on the sides of the CNWs [15]. In particular, as explained in the previous paragraph (figure 1), the CNWs grow thicker with decreasing pressure during the transition from CNW to nanorod growth, which should not occur when a higher proportion of a-C etchants is present in the plasma. Consequently, either surface chemistry on the substrate (which is impossible to probe with OES) or another effect must be the driving force of the CNW/nanorod growth transition.

3.3. A new growth model: Metal oxide incorporation dictates nanostructure morphology

Since the changes in morphology across the p-Q-parameter space cannot be explained by the plasma chemistry alone, in the following chemical analytics (XPS, SAM and Raman spectroscopy) are used to investigate the different morphologies' chemical composition, defects, and bond structure and their possible influence on nanostructure growth.

XPS was used to probe the chemical bond structure and composition of the observed morphologies. The C1s, O1s, N1s, Si2p, and Al2p core level transitions were recorded at every measured spot. For none of the measurements, a sufficient signal of N1s or Si2p was recorded, as expected. The Al2p signal of various morphologies can be found in figure 7. The peak at 74.7 eV is assigned to Al_2O_3 [50]. Neither pure aluminum nor aluminum carbide could be found. From nanoflakes to nanorods (and across the morphologies lying in between) the overall oxygen and aluminum content increase, while carbon decreases.

The C_{KVV} Auger peak of all the morphologies was recorded. Due to its origin, it can give some insight into the electronic structure of a sample. The so-called D-parameter is the width of this peak and is used in literature to determine the ratio of sp^2- to sp^3-hybridized carbon in several carbon allotropes [51–54]. The D-parameter is found to be between 20 and 21 eV and does not show any significant variation across any of the morphologies, apart from statistical deviation. This value of the D-parameter translates to 90%–100% sp^2-hybridized carbon in the probed area [54]. Although, slight changes in the ratio of sp^2- to sp^3-hybridized carbon are hardly possible to probe with this method, due to the energy resolution of the machine.
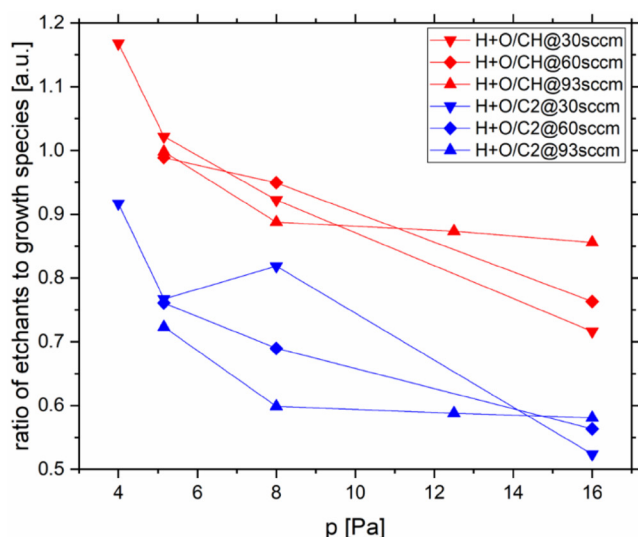
Figure 6. The ratios of etchants to growth species varying with pressure calculated from OES spectra. The ratios decrease with increasing pressure. This contradicts the growth model proposed in the literature, when considering the morphology evolution across the pressure range.

Figure 7. The Al2p signal of different morphologies measured by XPS. The signal increases from nanoflake to nanorod morphology.

After several XPS spectra were taken of samples from different processes, in which the same morphologies were produced at varying distance to the gas inlet (by changing pressure or carrier gas flow rate), it is apparent that the morphology of the CNWs is dependent on the aluminum content. Hence, similar morphologies will have comparable aluminum contents regardless of process parameters.

The effect of higher Al_2O_3 content on layer morphology can already be seen during the formation of the buffer layer. A buffer layer between the substrate layer and CNWs has been described in the literature [14, 16, 19] and was formed on every sample, regardless of morphology. Until now, the buffer layer has not been part of an in-depth investigation on morphology-controlled growth, but could in principle have an influence on early nucleation and therefore the resulting morphology. Figure 8 shows buffer layers of the three distinct morphologies of this work recorded with an ultra-high-resolution SEM (UHRSEM). All six images are taken from three samples of the same process after 15 min process time. After this time, the buffer layer has formed completely, and early CNW nucleation is observed in some parts of the samples. The buffer layer is smooth for nanoflakes and becomes increasingly porous and even fissures towards the nanorods morphology. As shown by XPS, Al_2O_3 content increases from nanoflakes to nanorods and, therefore, in the direction of increased fissuring. Hence, a likely cause for the disturbance of the buffer layers' structure is the incorporation of Al_2O_3 into the carbon matrix.

Within the process window, that can be realized in the set-up used, the initial nucleation of nanorods was always observed to come from CNWs and never from the buffer layer alone. The thicker the CNWs (at closer distances to the gas inlet or lower residence times) the earlier the nanorods grow on top of them. Therefore, it is reasonable to assume that there is a pure nanorod growth regime outside of the parameter space, that is not realizable in the current set-up.
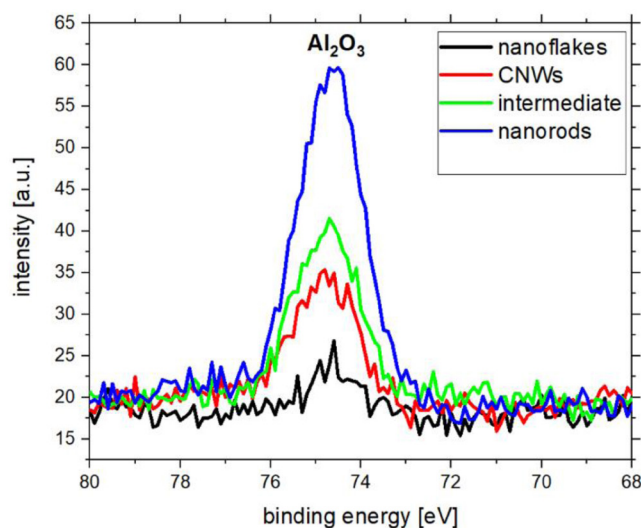
The progenitor CNWs of the CNW-nanorod intermediate and the nanorod morphology span across multiple cracks, so it seems they grow on top of the buffer layer, which then has little influence on nucleation and therefore morphology. Accordingly, for nanorods, nucleation sites are likely to be created through ion bombardment from the plasma as theorized by Kondo et al [16]. Contrary to this, for the CNW and nanoflake morphology, where the buffer layer becomes much smoother, nucleation seems to happen in the buffer layer. Nucleation can be observed exceptionally well at ultra-high-resolution. Here, the nucleation of flakes is likely enabled by surface stress [15, 20] at mismatch points in the graphitic buffer layer as proposed before [14]. A transition from nanoflakes to CNWs would then be enabled by the increase of fissuring in the buffer layer and therefore an increase in surface stress, promoting the formation of vertically well-aligned CNW nuclei.

As shown before by the transmission electron microscope measurements of Jain et al [55], by the SAM measurements of Giese et al [23] and by the fissuring of the buffer layer, the aluminum found within the layer by XPS is likely incorporated into the carbon matrix. To further investigate the dependence of aluminum content on morphology, SAM was employed. Similar to XPS, SAM can probe the bond structure and chemical composition of a sample, but with a much better lateral resolution, due to excitation with a focused electron beam. The CNW morphology was studied under this angle, to verify that Al_2O_3 is not only incorporated into the buffer layer but into the walls as well. The Auger peaks of C, O, Al and Si were recorded at nine different positions as shown in figure 9(a), of which eight (points 2–9) were placed alongside the growth direction of the wall, and one on the buffer layer (point 1). The Si signal acts as an indicator that mostly CNWs and not the buffer layer (by penetration of multiple walls) were measured. As expected, no Si signal was detected at points 2–9 owing to the extreme surface sensitivity (information depth ~5 nm at most) of the SAM technique. A substantial amount of 8.0 at% of aluminum is found in the buffer layer. The variation in
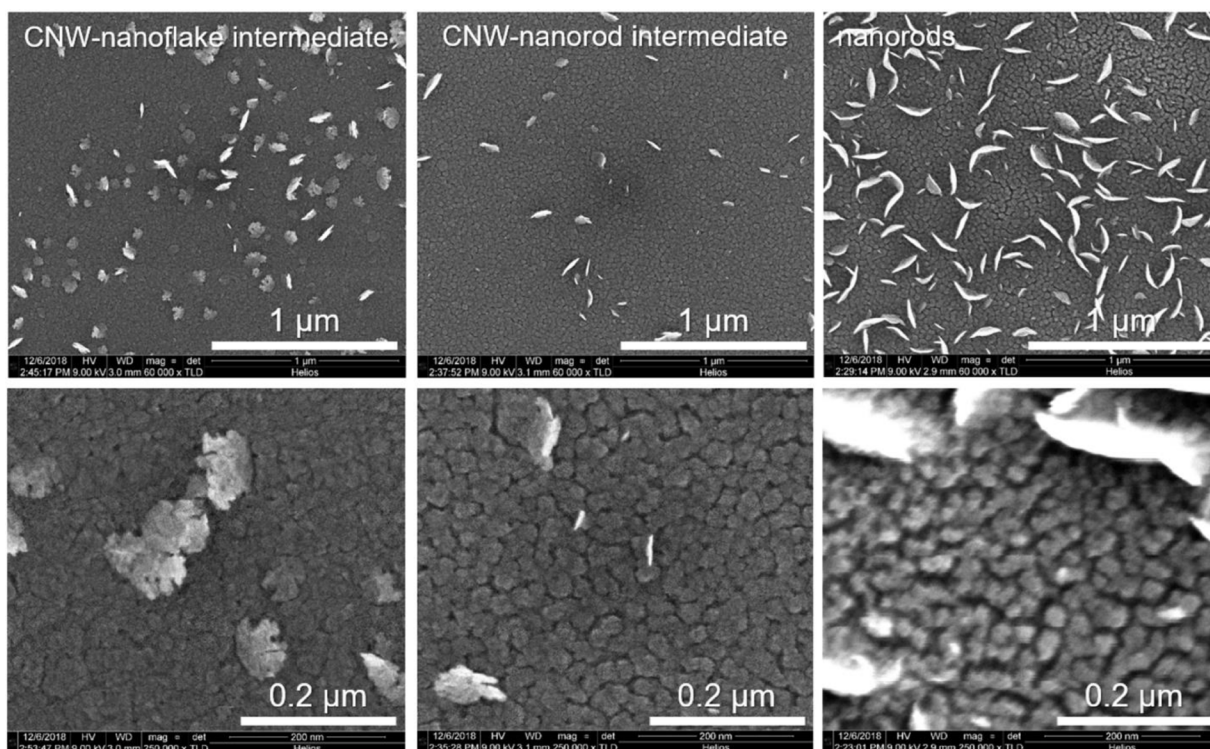
Figure 8. UHRSEM images of samples after only 15 min process time. The buffer layer is observable and grows more porous and even fissures from nanoflake to nanorod morphology.
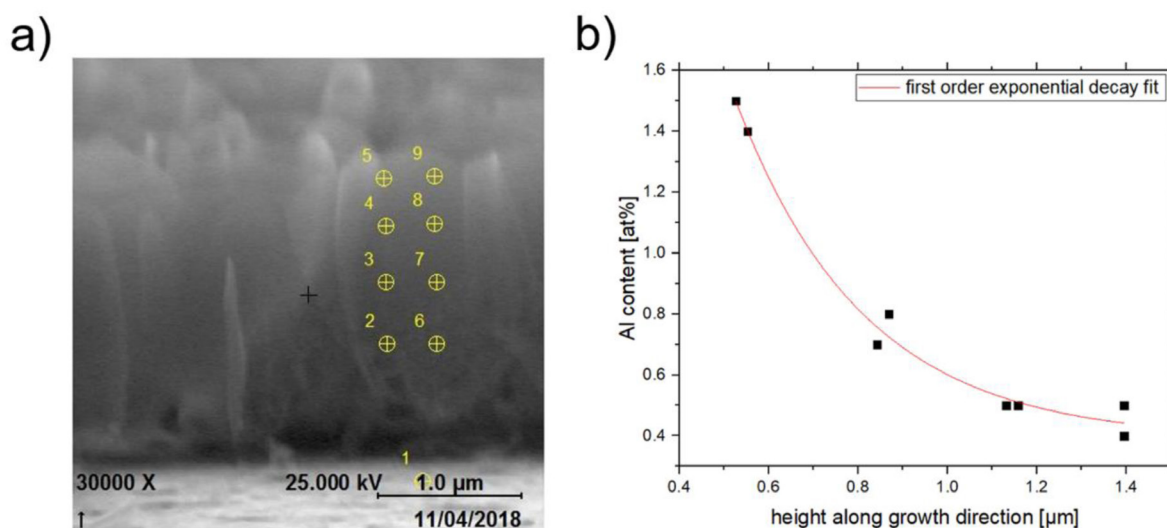

Figure 9. (a) SEM image of the CNW morphology under 90° tilt with marks indicating the measurement position of the SAM spectra. (b) Evaluation of the atomic percentage of aluminum within a CNW alongside its growth direction. Saturation of the Al content is expected at a certain height.

aluminum content alongside the growth direction of the wall is shown in figure 9(b). Less aluminum is incorporated at the top of the wall compared to the bottom, and the gradient can be fitted with a first order exponential decay function, which possibly saturates at a specific height.

Figure 10 shows UHRSEM cross-section images of individual CNWs, CNW-nanorod intermediates, and nanorods under a 45° tilt. The samples were produced in a single process. The height of all the morphologies is comparable. Therefore, it can be assumed that they are all in the same

state of growth. In general, the overall porosity (roughness) of the different morphologies increases from the nanoflake to the nanorod morphology, hence, showing the same trend as observed for the buffer layer. Additionally, the porosity seems to always increase from the top to the bottom of at least the CNW and CNW-nanorod intermediate morphology. For the nanorod morphology, the structure is remarkably fissured, which makes it hard to discern a porosity gradient alongside the growth direction. For the intermediates, shown in figure 10, one can see clearly that the nanorods form on top
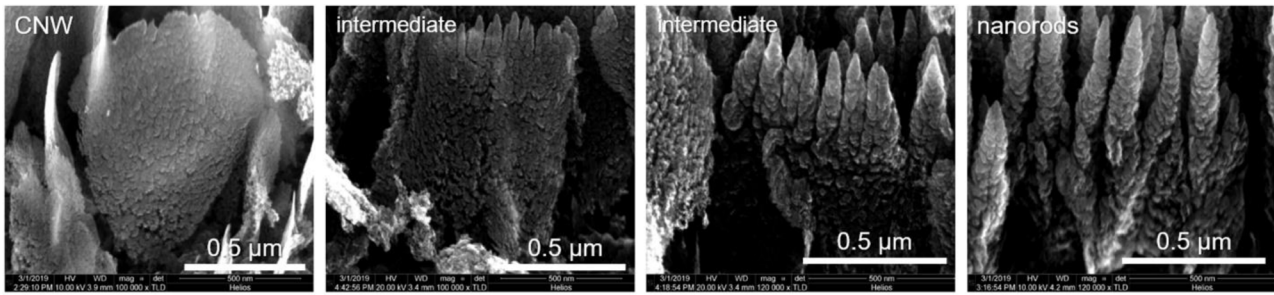
J. Phys. D: Appl. Phys. **53** (2020) 145206

S Tigges *et al*

Figure 10. UHRSEM images of samples under 45° tilt of the same process featuring different morphologies. The porosity of a wall increases from top to bottom. The overall porosity of the morphologies increases noticeably from CNWs to nanorods.

Table 2. Atomic percentages of carbon, oxygen and aluminum taken from XPS spectra of different morphologies.

Morphology	Carbon content (at%)	Oxygen content (at%)	Aluminum content (at%)
Nanoflakes	95.2	4.7	0.1
CNWs	95.1	4.3	0.6
CNW-nanorod intermediate	93.8	5.4	0.8
Nanorods	89.1	9.1	1.7

the walls, as stated earlier. Here, by looking at the transparency of the walls for the electron beam, it is also apparent, that the structure thickness increases immensely from CNWs to nanorods.

The gradient of aluminum content alongside the CNW observed in figure 9 coincides with the observation of increasing porosity of a wall towards its bottom described above. Assuming that Al_2O_3 is incorporated into the carbon matrix, it would distort the carbon lattice creating defects and fissures, due to mismatch of lattice constants. Furthermore, the overall porosity of the morphologies increases from nanoflakes to nanorods, as observed above, while the aluminum content increases as well, as shown in table 2. The general observation of increased porosity and fissuring in regions, where the aluminum content increases, supports the claim of incorporation and lattice distortion. More incorporation would then result in more distortion. Distortion can be measured in terms of defect density and defect type by Raman spectroscopy owing to its ability to probe the electronic structure of a sample, which is shown in the following paragraph.

A morphological transition from nanoflakes to CNWs to nanorods should be observable by Raman spectroscopy. In typical CNW samples, in the range of 1000–3200 cm^{-1}, 6 peaks may be observed, namely D (~1350 cm^{-1}), G (~1590 cm^{-1}), D′ (~1620 cm^{-1}), D + D″ (~2500 cm^{-1}), 2D (~2700 cm^{-1}, also called G′) and D + D′ (~3000 cm^{-1}). The origin of these peaks is described in detail in the work of Ferrari *et al* [56]. The ratio of intensity of the D to G peak (I(D)/I(G)) gives insight into the number of defects present in a sample (in terms of average inter-defect distance or rather crystallite size) via the Tuinstra–Koenig relation [57], which was later adjusted by Cançado *et al*, due to the excitation energy dependent dispersion of the D peak [58]. For this, the degree of amorphization must be determined by the three-stage model proposed by Ferrari and Robertson [59], in which I(D)/I(G) combined with
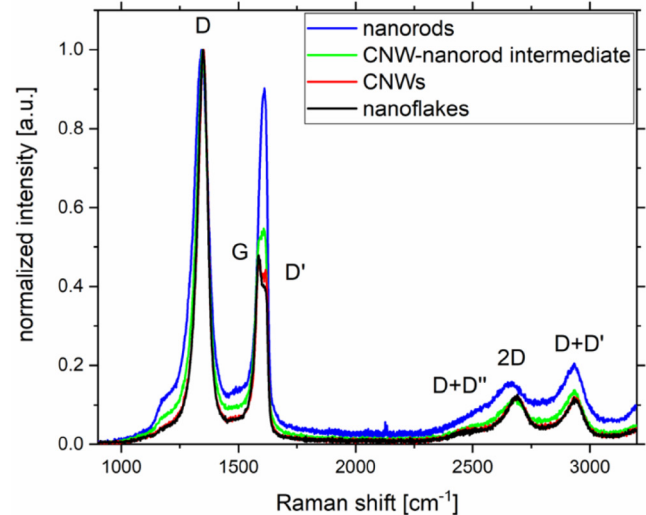

Figure 11. Raman spectra of different morphologies, including the identification of all relevant peaks. A clear difference in the spectra of the nanostructures is observed.

the position of the G peak (Pos(G)) reflects upon the nature of hybridization of carbon bonds in the sample.

In figure 11 four Raman spectra of different morphologies are shown. A process time-dependent variation in the spectra is not observed (SI figure 1), further proving the existence of growth zones, which was introduced earlier. CNWs and nanoflakes exhibit the typical spectrum, which was observed in literature before [60, 61]. The D′ peak is clearly visible and distinguishable from the G peak, which when combined with Pos(G) (between 1594 and 1597 cm^{-1}) and FWHM of G (approx. 40 cm^{-1} for all of the spectra) indicates stage 1 amorphization of the CNW and nanoflake morphology [60]. The large I(D)/I(G) ratio results in a value of L_D (inter defect distance) of around 9 nm ± 1 nm, which also shows that these two morphologies are in stage 1, as the transition into stage 2 generally happens at an inter-defect distance of approx. 3.5 nm [58]. Approaching the transition to stage 2 would lead to a shift of Pos(G) to higher wavenumbers, as could be interpreted into the trend from nanoflakes/CNWs to nanorods within the presented data, but it should also be accompanied by an increase in I(D)/I(G) [59]. The opposite is the case here. Using the three-stage model, this is not explainable.

Eckmann *et al* linked the ratio of I(D)/I(D′) to the defect type using ion-irradiated and fluorinated graphene samples

J. Phys. D: Appl. Phys. 53 (2020) 145206
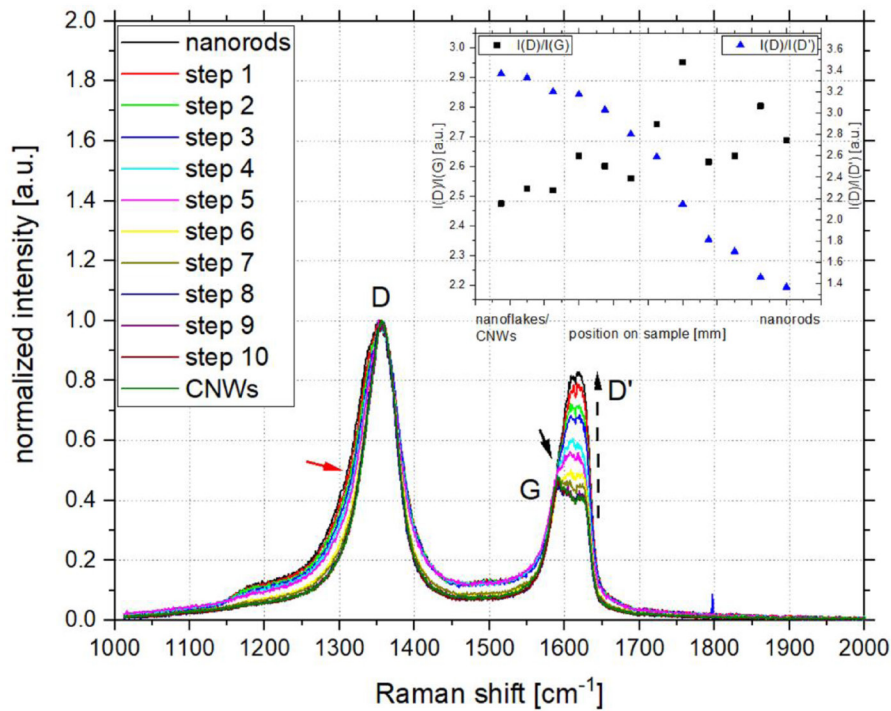
S Tigges *et al*

Figure 12. Raman spectra taken of two samples from the same process at a different distance to the gas inlet. Twelve points alongside the direction of the gas flow were measured on the samples, which display the evolution of D, G, and D′ peaks from CNW to nanorod morphology. The in-set shows the calculated values for $I(D)/I(G)$ (black rectangles) and $I(D)/I(D')$ (blue triangles). While $I(D)/I(G)$ stays comparable, $I(D)/I(D')$ decreases significantly (dotted arrow). With decreasing $I(D)/I(D')$, the D peak becomes broader (red arrow) forming a shoulder on the left flank, while the G peak stays similar, also forming a shoulder on the left flank (black arrow) of the convoluted G/D′-signal.

[36]. With this, it becomes possible to not only quantify the state of amorphization of a sample by the three-stage model but also to identify the most dominant type of Raman-active defect within a sample. The $I(D)/I(D')$ ratios of their samples as well as of data from the literature is at a maximum for sp^3-type defects at around 13, decreases to 7 for vacancy-like defects and is lowest at 3.5 for boundary-like defects. These boundary-like defects are most common in CNWs and nanoflakes because of their sharp, exposed edges [60]. *Ab initio* calculations by Venezuela *et al* revealed the $I(D)/I(D')$ ratios of two more defect types, the hopping defect at a ratio of 10 and the sp^3-hybridized on-site defect (an out-of-plane carbon atom) at 1.3 [62]. These results deviate from the experimentally measured values previously reported in the literature, due to the limitations imposed on the theoretical model as explained by Eckmann *et al* [36], but are still taken into consideration in a qualitative manner similar to the work of Ghosh *et al* [60].

The interpretation of the Raman spectra based on defective graphene by Eckmann *et al* [36] may provide a reasonable explanation for the observed trends. When fitting the obtained spectra with the method provided by Eckmann *et al* [36], a decreasing trend in the $I(D)/I(D')$ ratios from 3.4 to 1.4 is observed when going from nanoflake/CNW to nanorod morphology, while $I(D)/I(G)$ changes from 2.5 to 2.8. Trends for D, G and D′ peaks are more clearly observable in figure 12, where several Raman spectra in steps of 1.5 mm (from CNWs to nanorods) were taken across two samples, that were grown

in the same process. The $I(D)/I(G)$ as well as $I(D)/I(D')$ ratios of these spectra were calculated and are shown in the inset of figure 12. Contrary to spectra of various carbon allotropes with different degrees of amorphization frequently observed in the literature, the position of the G peak in figure 12 seems to only shift slightly to higher wavenumbers, while $I(D')$ increases significantly. The G peak eventually forms a small shoulder on the left flank of the convoluted signal (black arrow in figure 12). Simultaneously, the D peak becomes broader (also forming a shoulder at the left flank; red arrow in figure 12), and the 2D peak broadens and shifts to lower wavenumbers (observable in figures 11 and SI figure 2). In general, the broadening of these peaks indicates amorphization [56, 59]. D peak broadening may also be a sign for changes in the defect type of the sample, as the formation of a shoulder on the flank of the D peak, which indicates a transition from edge few layer graphene to edge graphite [56], might result from the walls becoming thicker towards the nanorod morphology. The $I(D)/I(D')$ value starts at approx. 3.4 for nanoflakes and decreases steadily until reaching approx. 1.4 for nanorods. The same trend is observed for the buffer layer (not shown here). As $I(D)/I(D')$ decreases the defect type changes from boundary-like defects (nanoflakes and CNWs), typically observed in CNW samples, to sp^3-hybridized on-site defects [36, 62] or mono-vacancy defects [63]. During this, the amount of defects increases slightly ($I(D)/I(G)$ increases from 2.5 to 2.8), without inducing a stage transition into stage 2, as an L_D of 7 nm $\pm$ 1 nm can be calculated for nanorods. Under

the assumption that Eckmann *et al*'s model upholds for this morphology transition, the changes in defect type and number are reasonable, as the general structure of the layer changes from walls to rods, losing the edges in the process, while becoming increasingly porous. A similar trend in $I(D)/I(D')$ has been observed by Zandiatashbar *et al*, where the oxygen plasma treatment of defective single-layer graphene resulted in the formation of nanopores in the sheet [64].

Therefore, contrary to the morphology transition from nanoflakes to CNWs, which is enabled by the fissuring of the buffer layer, the transition from CNWs to nanorods is a result of the increased incorporation of Al_2O_3 into the walls. Al_2O_3 incorporation leads to an increase in sp^3-hybridized on-site defects or mono-vacancy defects, which inhibit the surface diffusion of carbon on the sides of the walls. Due to this inhibition, carbon is deposited on the sides of the walls, increasing the wall thickness and porosity until a morphology transition from thick CNWs to nanorods is energetically more favorable.

4. Conclusion

Hybrid CNWs consisting of metal oxide nanoparticles incorporated in a carbon matrix material were synthesized in a single-step process from a metal-organic precursor. Substantial morphological changes along the direction of the gas flow are observed across all samples. The origin of these changes is the residence time of precursor in the plasma, which influences the degree of precursor dissociation and leads to specific growth zones. This finding is supported by the fact that the morphology does not change for extended growth time (no time-dependent structures).

In contrast to previous growth models proposed in literature [13, 15], the deposition of the different morphologies from a metal-organic precursor cannot solely be explained by the plasma chemistry alone.

SEM, SAM, XPS, OES, and Raman spectroscopy results indicate a decisive connection between Al_2O_3 content and layer morphology. Hydrocarbons are still presumed to be the primary growth species of every carbon structure resulting from the dissociation of acetone (in agreement with Vizireanu *et al* [25]), while Al_2O_3 incorporation dictates layer morphology. With the observation of a variation in the porosity of the morphologies made in SAM, it is reasonable to assume, that the incorporation of Al_2O_3 observed via SAM and XPS disturbs the lattice of the carbon matrix, promoting defects. For the transition from planar nanoflake to vertical CNW growth, the increasing fissuring of the buffer layer, caused by increased aluminum oxide incorporation, might lead to increased surface stress, ultimately resulting in a larger amount of vertically well-aligned CNW nuclei [14, 15]. For the transition from CNWs to nanorods, it is observed that the wall thickness and porosity increase noticeably. As mentioned in the physical analysis part of the results, increasing wall thickness must be related to an increased deposition of out-of-plane carbon at the side of the walls (i.e. on-site defects). At low-temperatures, surface diffusion energies play a significant role in nanostructure formation [22], and an sp^3-hybridized

on-site defect or a vacancy on the sides of a CNW would then increase the probability of adsorption of carbon atoms in the vicinity of the defect, thus, decreasing diffusion length and promoting out-of-plane growth [18]. Since in the Raman spectra, the $I(D)/I(G)$ ratio only slightly increases from nanoflakes to nanorods, the increased incorporation of Al_2O_3 observed with XPS only leads to slightly more defects, and instead changes the dominant type of defect, enabling the transition from CNW to nanorod growth.

The results presented above could be transferred to the deposition of carbon nanostructures incorporated with other metals and metal oxides in the presented set-up by use of a different metal acetylacetonate as precursor. Furthermore, our results could be interesting for the understanding of the growth mechanisms from other one-step deposition methods (i.e. the chemical vapor synthesis of Fe/C [65] for application in NOx conversion [66]).

ORCID iDs

Sebastian Tigges ⬤ https://orcid.org/0000-0002-4313-846X
Nicolas Wöhrl ⬤ https://orcid.org/0000-0002-4232-9379
Ulrich Hagemann ⬤ https://orcid.org/0000-0002-1880-6550
Axel Lorke ⬤ https://orcid.org/0000-0002-0405-7720

References

[1] Wu Y, Qiao P, Chong T and Shen Z 2002 Carbon nanowalls grown by microwave plasma enhanced chemical vapor deposition *Adv. Mater.* **14** 64–7
[2] Giorgi L, Makris T, Giorgi R, Lisi N and Salernitano E 2007 Electrochemical properties of carbon nanowalls synthesized by HF-CVD *Sensors Actuators* B **126** 144–52
[3] Lehmann K, Yurchenko O, Melke J, Fischer A and Urban G 2018 High electrocatalytic activity of metal-free and non-doped hierarchical carbon nanowalls towards oxygen reduction reaction *Electrochim. Acta* **269** 657–67
[4] Machino T, Takeuchi W, Kano H, Hiramatsu M and Hori M 2009 Synthesis of platinum nanoparticles on two-dimensional carbon nanostructures with an ultrahigh aspect ratio employing supercritical fluid chemical vapor deposition process *Appl. Phys. Express* **2** 025001
[5] Krivchenko V A, Itkis D M, Evlashin S A, Semenenko D A, Goodilin E A, Rakhimov A T, Stepanov A S, Suetin N V, Pilevsky A A and Voronin P V 2012 Carbon nanowalls decorated with silicon for lithium-ion batteries *Carbon* **50** 1438–42
[6] Wu J, Shao Y, Wang B, Ostrikov K, Feng J and Cheng Q 2016 Plasma-produced vertical carbonous nanoflakes for Li-ion batteries *Plasma Process. Polym.* **13** 1008–14

J. Phys. D: Appl. Phys. **53** (2020) 145206

S Tigges *et al*

[7] Tanaike O, Kitada N, Yoshimura H, Hatori H, Kojima K and Tachibana M 2009 Lithium insertion behavior of carbon nanowalls by dc plasma CVD and its heat-treatment effect *Solid State Ion.* **180** 381–5

[8] Wang J and Ito T 2007 CVD growth and field emission characteristics of nano-structured films composed of vertically standing and mutually intersecting nano-carbon sheets *Diam. Relat. Mater.* **16** 589–93

[9] Hojati-Talemi P and Simon G P 2011 Field emission study of graphene nanowalls prepared by microwave-plasma method *Carbon* **49** 2875–7

[10] Jothiramalingam Sankaran K *et al* 2018 Self-organized multi-layered graphene–boron-doped diamond hybrid nanowalls for high-performance electron emission devices *Nanoscale* **10** 1345–55

[11] Hiramatsu M and Hori M 2010 *Carbon Nanowalls: Synthesis and Emerging Applications* (Berlin: Springer)

[12] Bo Z, Yang Y, Chen J, Yu K, Yan J and Cen K 2013 Plasma-enhanced chemical vapor deposition synthesis of vertically oriented graphene nanosheets *Nanoscale* **5** 5180–204

[13] Santhosh N M, Filipič G, Tatarova E, Baranov O, Kondo H, Sekine M, Hori M, Ostrikov K and Cvelbar U 2018 Oriented carbon nanostructures by plasma processing: recent advances and future challenges *Micromachines* **9** 565

[14] Zhao J, Shaygan M, Eckert J, Meyyappan M and Rümmeli M H 2014 A growth mechanism for free-standing vertical graphene *Nano Lett.* **14** 3064–71

[15] Zhu M, Wang J, Holloway B C, Outlaw R A, Zhao X, Hou K, Shutthanandan V and Manos D M 2007 A mechanism for carbon nanosheet formation *Carbon* **45** 2229–34

[16] Kondo S, Kawai S, Takeuchi W, Yamakawa K, Den S, Kano H, Hiramatsu M and Hori M 2009 Initial growth process of carbon nanowalls synthesized by radical injection plasma-enhanced chemical vapor deposition *J. Appl. Phys.* **106** 094302

[17] Davami K, Shaygan M, Kheirabi N, Zhao J, Kovalenko D A, Rümmeli M H, Opitz J, Cuniberti G, Lee J-S and Meyyappan M 2014 Synthesis and characterization of carbon nanowalls on different substrates by radio frequency plasma enhanced chemical vapor deposition *Carbon* **72** 372–80

[18] Baranov O, Levchenko I, Xu S, Lim J W M, Cvelbar U and Bazaka K 2018 Formation of vertically oriented graphenes: what are the key drivers of growth? *2D Mater.* **5** 044002

[19] Bo Z, Mao S, Han Z J, Cen K, Chen J and Ostrikov K 2015 Emerging energy and environmental applications of vertically-oriented graphenes *Chem. Soc. Rev.* **44** 2108–21

[20] Malesevic A, Vitchev R, Schouteden K, Volodin A, Zhang L, Tendeloo G V, Vanhulsel A and Haesendonck C V 2008 Synthesis of few-layer graphene via microwave plasma-enhanced chemical vapour deposition *Nanotechnology* **19** 305604

[21] Wu X X and Yang X X 2002 Effects of localized electric field on the growth of carbon nanowalls *Nano Lett.* **2** 355–9

[22] Levchenko I, Keidar M, Xu S, Kersten H and Ostrikov K 2013 Low-temperature plasmas in carbon nanostructure synthesis *J. Vac. Sci. Technol.* B **31** 050801

[23] Giese A, Schipporeit S, Buck V and Wöhrl N 2018 Synthesis of carbon nanowalls from a single-source metal-organic precursor *Beilstein J. Nanotechnol.* **9** 1895–905

[24] Levchenko I, Ostrikov K, Rider A E, Tam E, Vladimirov S V and Xu S 2007 Growth kinetics of carbon nanowall-like structures in low-temperature plasmas *Phys. Plasmas* **14** 063502

[25] Vizireanu S, Stoica S D, Luculescu C, Nistor L C, Mitu B and Dinescu G 2010 Plasma techniques for nanostructured carbon materials synthesis. A case study: carbon nanowall growth by low pressure expanding RF plasma *Plasma Sources Sci. Technol.* **19** 034016

[26] Cho H J, Kondo H, Ishikawa K, Sekine M, Hiramatsu M and Hori M 2014 Density control of carbon nanowalls grown by CH₄/H₂ plasma and their electrical properties *Carbon* **68** 380–8

[27] Wang J, Zhu M, Outlaw R A, Zhao X, Manos D M and Holloway B C 2004 Synthesis of carbon nanosheets by inductively coupled radio-frequency plasma enhanced chemical vapor deposition *Carbon* **42** 2867–72

[28] Bo Z, Yu K, Lu G, Wang P, Mao S and Chen J 2011 Understanding growth of carbon nanowalls at atmospheric pressure using normal glow discharge plasma-enhanced chemical vapor deposition *Carbon* **49** 1849–58

[29] Lehmann K, Yurchenko O and Urban G 2016 Effect of the aromatic precursor flow rate on the morphology and properties of carbon nanostructures in plasma enhanced chemical vapor deposition *RSC Adv.* **6** 32779–88

[30] Lehmann K, Yurchenko O, Heilemann A, Vierrath S, Zielke L, Thiele S, Fischer A and Urban G 2017 High surface hierarchical carbon nanowalls synthesized by plasma deposition using an aromatic precursor *Carbon* **118** 578–87

[31] Jain H G, Karacuban H, Krix D, Becker H-W, Nienhaus H and Buck V 2011 Carbon nanowalls deposited by inductively coupled plasma enhanced chemical vapor deposition using aluminum acetylacetonate as precursor *Carbon* **49** 4987–95

[32] Ostrikov K, Neyts E C and Meyyappan M 2013 Plasma nanoscience: from nano-solids in plasmas to nano-plasmas in solids *Adv. Phys.* **62** 113–224

[33] Kobayashi T, Hirakuri K K, Mutsukura N and Machi Y 1999 Synthesis of CVD diamond at atmospheric pressure using the hot-filament CVD method *Diam. Relat. Mater.* **8** 1057–60

[34] Miller P A, Hebner G A, Greenberg K E, Pochan P D and Aragon B P 1995 An inductively coupled plasma source for the gaseous electronics conference RF reference cell *J. Res. Natl Inst. Stand Technol.* **100** 427–39

[35] Kadetov V A 2004 Diagnostics and modeling of an inductively coupled radio frequency discharge in hydrogen *Dissertation*

[36] Eckmann A, Felten A, Mishchenko A, Britnell L, Krupke R, Novoselov K S and Casiraghi C 2012 Probing the nature of defects in graphene by Raman spectroscopy *Nano Lett.* **12** 3925–30

[37] Kurita S, Yoshimura A, Kawamoto H, Uchida T, Kojima K, Tachibana M, Molina-Morales P and Nakai H 2005 Raman spectra of carbon nanowalls grown by plasma-enhanced chemical vapor deposition *J. Appl. Phys.* **97** 104320

[38] Vizireanu S, Nistor L, Haupt M, Katzenmaier V, Oehr C and Dinescu G 2008 Carbon nanowalls growth by radiofrequency plasma-beam-enhanced chemical vapor deposition *Plasma Process. Polym.* **5** 263–8

[39] Teii K, Shimada S, Nakashima M and Chuang A T H 2009 Synthesis and electrical characterization of N-type carbon nanowalls *J. Appl. Phys.* **106** 084303

[40] Takeuchi W, Sasaki H, Kato S, Takashima S, Hiramatsu M and Hori M 2009 Development of measurement technique for carbon atoms employing vacuum ultraviolet absorption spectroscopy with a microdischarge hollow-cathode lamp and its application to diagnostics of nanographene sheet material formation plasmas *J. Appl. Phys.* **105** 113305

[41] Sandoz-Rosado E *et al* 2014 Vertical graphene by plasma-enhanced chemical vapor deposition: correlation of plasma conditions and growth characteristics *J. Mater. Res.* **29** 417–25

[42] Acosta Gentoiu M, Betancourt-Riera R, Vizireanu S, Burducea I, Marascu V, Stoica S D, Bita B I, Dinescu G and Riera R 2017 Morphology, microstructure, and hydrogen content of carbon nanostructures obtained by PECVD at various temperatures *J. Nanomater.* **2017** 1374973

[43] Shang N G, Au F C K, Meng X M, Lee C S, Bello I and Lee S T 2002 Uniform carbon nanoflake films and their field emissions *Chem. Phys. Lett.* **358** 187–91

[44] Coburn J W and Chen M 1980 Optical emission spectroscopy of reactive plasmas: a method for correlating emission intensities to reactive particle density *J. Appl. Phys.* **51** 3134–6

[45] Charles R G, Hoene J V and Hickam W M 1958 Thermal decomposition of metal acetylacetonates: mass spectrometer studies *J. Phys. Chem.* **62** 1098–101

[46] Charles R G, Hickam W M and Hoene J V 1959 The pyrolysis of acetylacetone *J. Phys. Chem.* **63** 2083–4

[47] Kim J S, Marzouk H A, Reucroft P J, Robertson J D and Hamrin C E 1993 Effect of water vapor on the growth of aluminum oxide films by low pressure chemical vapor deposition *Thin Solid Films* **230** 156–9

[48] Rodriguez P, Caussat B, Iltis X, Ablitzer C and Brothier M 2012 Alumina coatings on silica powders by fluidized bed chemical vapor deposition from aluminium acetylacetonate *Chem. Eng. J.* **211–2** 68–76

[49] Tsyganova E I and Dyagileva L M 1996 The reactivity of metal β-diketonates in the thermal decomposition reaction *Russ. Chem. Rev.* **65** 315

[50] Moulder J F 1992 *Handbook of X-Ray Photoelectron Spectroscopy: a Reference Book of Standard Spectra for Identification and Interpretation of XPS Data* (Eden Prairie, MN: Physical Electronics Division, Perkin-Elmer Corporation)

[51] Mizokawa Y, Miyasato T, Nakamura S, Geib K M and Wilmsen C W 1987 Comparison of the CKLL first-derivative auger spectra from XPS and AES using diamond, graphite, SiC and diamond-like-carbon films *Surf. Sci.* **182** 431–8

[52] Mizokawa Y, Miyasato T, Nakamura S, Geib K M and Wilmsen C W 1987 The C KLL first-derivative x-ray photoelectron spectroscopy spectra as a fingerprint of the carbon state and the characterization of diamondlike carbon films *J. Vac. Sci. Technol.* A **5** 2809–813

[53] Speranza G and Laidani N 2004 Measurement of the relative abundance of Sp^2 and Sp^3 hybridised atoms in carbon based materials by XPS: a critical approach. Part I *Diam. Relat. Mater.* **13** 445–50

[54] Kaciulis S 2012 Spectroscopy of carbon: from diamond to nitride films *Surf. Interface Anal.* **44** 1155–61

[55] Jain H G 2012 Synthesis and characterization of carbon nanowalls by ICP-CVD using aluminium-acetylacetonate precursor *Dissertation*

[56] Ferrari A C and Basko D M 2013 Raman spectroscopy as a versatile tool for studying the properties of graphene *Nat. Nanotechnol.* **8** 235–46

[57] Tuinstra F and Koenig J L 1970 Raman spectrum of graphite *J. Chem. Phys.* **53** 1126–30

[58] Cançado L G, Jorio A, Ferreira E H M, Stavale F, Achete C A, Capaz R B, Moutinho M V O, Lombardo A, Kulmala T S and Ferrari A C 2011 Quantifying defects in graphene via Raman spectroscopy at different excitation energies *Nano Lett.* **11** 3190–6

[59] Ferrari A C and Robertson J 2000 Interpretation of Raman spectra of disordered and amorphous carbon *Phys. Rev.* B **61** 14095–107

[60] Ghosh S, Ganesan K, Polaki S R, Ravindran T R, Krishna N G, Kamruddin M and Tyagi A K 2014 Evolution and defect analysis of vertical graphene nanosheets *J. Raman Spectrosc.* **45** 642–9

[61] Ni Z H, Fan H M, Feng Y P, Shen Z X, Yang B J and Wu Y H 2006 Raman spectroscopic investigation of carbon nanowalls *J. Chem. Phys.* **124** 204703

[62] Venezuela P, Lazzeri M and Mauri F 2011 Theory of double-resonant Raman spectra in graphene: intensity and line shape of defect-induced and two-phonon bands *Phys. Rev.* B **84** 035433

[63] Jiang J, Pachter R, Mehmood F, Islam A E, Maruyama B and Boeckl J J 2015 A Raman spectroscopy signature for characterizing defective single-layer graphene: defect-induced $I(D)/I(D')$ intensity ratio by theoretical analysis *Carbon* **90** 53–62

[64] Zandiatashbar A, Lee G-H, An S J, Lee S, Mathew N, Terrones M, Hayashi T, Picu C R, Hone J and Koratkar N 2014 Effect of defects on the intrinsic strength and stiffness of graphene *Nat. Commun.* **5** 3186

[65] Enz T, Winterer M, Stahl B, Bhattacharya S, Miehe G, Foster K, Fasel C and Hahn H 2006 Structure and magnetic properties of iron nanoparticles stabilized in carbon *J. Appl. Phys.* **99** 044306

[66] Busch M, Kompch A, Suleiman S, Notthoff C, Bergmann U, Theissmann R, Atakan B and Winterer M 2015 NO$_x$ conversion properties of a novel material: iron nanoparticles stabilized in carbon *Appl. Catal.* B **166–7** 211–6